# *Unraveling the Cooperative Mechanism of Visible-light Absorption in Bulk N,Nb Codoped $TiO_2$ nanopowders*

Chiara Marchiori[a], Giovanni Di Liberto[a], Guido Soliveri[a], Laura Loconte[a], Leonardo Lo Presti[a,b,c,*], Daniela Meroni[a,d,*], Michele Ceotto[a,d], Cesare Oliva[a,d], Serena Cappelli[a], Giuseppe Cappelletti[a,d], Chiara Aieta[a], Silvia Ardizzone[a,d]

[a] Dipartimento di Chimica, Università degli Studi di Milano, Via Golgi 19, 20133 Milano, Italy

[b] Istituto di Scienze e Tecnologie Molecolari, Italian CNR, Via Golgi 19, 20133 Milano, Italy

[c] Center for Materials Crystallography, Aarhus University, Langelandsgade 140, 8000 Aarhus, Denmark

[d] Consorzio Interuniversitario Nazionale per la Scienza e la Tecnologia dei Materiali (INSTM), Via Giusti 9, 50121 Firenze, Italy

To whom correspondence should be addressed: daniela.meroni@unimi.it; leonardo.lopresti@unimi.it tel. +39 0250314219; fax: +39 0250314228

**Please cite this work as:**

**C. Marchiori, G. Di Liberto, G. Soliveri, L. Loconte, L. Lo Presti, D. Meroni, M. Ceotto, C. Oliva, S. Cappelli, G. Cappelletti, C. Aieta, S. Ardizzone,**

***J. Phys. Chem. C*, 2014, 118 (41), pp 24152–24164**

**ABSTRACT**

N,Nb-codoping has recently been proposed as a promising strategy to enhance the activity of nanostructured $TiO_2$ under visible irradiation. Here, we suggest a possible electronic mechanism to account for the observed visible absorption improvement. The effects of N and Nb species on the electronic, crystallographic and morphological properties of $TiO_2$ were deeply investigated both experimentally (HR-XRPD, EXAFS, EDX, BET, SEM, EPR, DRS) and theoretically (DFT). We found a significant synergism between N and Nb species, while EXAFS, HR-XRPD and DFT simulations provided compelling evidence for the Nb substitutional position in anatase. At variance with interstitial, substitutional Nb can transfer an electron to low-energy valence states of the N codopant near the valence band. This intrinsic charge compensation mechanism is substantiated by EPR, that shows a reduction of the paramagnetic bulk N species signal in N,Nb-codoped samples. DRS analysis of N,Nb-codoped samples shows a slight reduction of the apparent band gap and a significantly increased visible-light absorbance. This effect is due to the shallow mid-gap states created by Nb (below conduction band) and N (above valence band). DFT results suggest that substitutional Nb ions transfer electrons to low-lying guest N states within the band gap, eventually enhancing the light absorption.

**KEYWORDS**

Nb,N-doped $TiO_2$, microstructure, nanostructure, point defects, DFT calculations, EPR measurements

## 1. INTRODUCTION

Titanium dioxide has been the subject of extensive research in recent years due to its relevant photochemical and photophysical properties combined with its natural abundance, low cost and superior chemical and photo-stability.[1] The nanocrystalline $TiO_2$ applications are quite numerous and span from photocatalysis, self-cleaning and antifogging devices to solar energy conversion and photoelectrochemical water splitting.[2-4]

Due to its wide band-gap ( > 3 eV), however, the $TiO_2$ photoactivity is restricted to the UV-region, which represents only less than 5% of the solar spectrum. Several approaches have been developed to promote the utilization of visible light ($\lambda > 400$ nm) by the $TiO_2$-based materials. Two main different possibilities have been proposed depending on the final application, either doping by p-block nonmetal species (N, C, S, P etc.) or promoting the material by metal cations[5].

In the case of nonmetal species the synthesis of N-doped $TiO_2$ has raised great interest and has become one of the most studied approaches to red shift the oxide light absorption.[6-7] N-doping induces a visible light absorption by creating localized mid-gap states. It has been observed that both the structural and the electronic picture of these systems are largely affected by the conditions adopted for the sample synthesis and by the nature of the N source.[8-9] Actually, these factors control the material microstructure, that in turn determines the concentration and nature of both extrinsic and intrinsic point defects. As for the latter, it is known that oxygen vacancies, $V_O^{\bullet\bullet}$, whose formation is favored by N doping[10], might reduce neighboring Ti ions and determine the formation of new gap states just below the conduction band (CB). It is believed that such defect-induced states could play a crucial role in enhancing the visible-light activity of N-doped $TiO_2$.[11-13] However, such shallow mid-gap levels can also act as recombination centers for photogenerated charge carriers, lowering the quantum efficiency of the photoinduced process.[11, 14] Further, the limited structural stability of N-doped $TiO_2$ represents another unresolved issue.[7, 15]

As for cationic dopants, the use of several metals of the first transition series has been

proposed. However, the enhanced absorption in the visible region has not always been accompanied by a significant improvement of the material photocatalytic performance. Rather, even detrimental effects were observed in some cases.[16] The doping effects are somehow different in the case of $TiO_2$ doped with high valence Sb(V) ($d^{10}$), Ta(V) ($d^0$) or Nb (V) ($d^0$) ions. The latter has been reported to promote both the photocatalytic activity and water splitting processes[17-18], even when combined with other lower valence transition cations[19]. More importantly, the technological relevance of Nb-promoted $TiO_2$ materials goes beyond classical photocatalytical and photoelectrochemical applications, as they have recently raised significant attention for the development of transparent conductive oxides. Specifically, it has been reported that Nb-$TiO_2$ can show an electronic conductivity comparable to that of the classic transparent conductive systems (indium tin oxide, fluorine tin oxide), while maintaining optimal visible transparency.[20-21] Such materials have received considerable attention also for the development of highly efficient photoanodes in dye-sensitized solar cells showing a reduced recombination loss and increased electron injection.[22-23]

The structural, electronic and defective properties of Nb-promoted $TiO_2$ systems play a major role in determining their final photoactivity. Two mechanisms have been proposed to account for the charge compensation of $Nb^{5+}$ introduced in the $TiO_2$ lattice. One involves the creation of $Ti^{3+}$ by excess electrons introduced by a mechanism of valence induction, while the other suggests the creation of one Ti cation vacancy per four Nb introduced. Donor mid-gap states are usually quite deep within the gap, and they may be responsible for a faster electron-hole recombination.[24] Codoping is a possible way to make these states less deep and more shallow into the band gap. More specifically, compensating codoping of $TiO_2$ with nonmetals and transition metals is a highly promising way to generate second-generation photocatalysts, where the apparent band gap decrease occurs without increasing the electron-hole recombination rate.[25-29] Density functional theory (DFT) calculations have indeed shown a correlated electronic effect between the host metal and the N within the $TiO_2$ lattice, suggesting a possible increase in the photocatalytic performance of the

material.[7, 26, 30-32] Marquez studied the structural and electronic properties of W, N codoped titania observing enhanced photocatalytic properties.[33] Significant results have been reported also in the case of V, N and Fe, N titania systems.[34-35]

Studies concerning the co-promotion of $TiO_2$ by N and Nb species are scarce although the simultaneous presence of species might intrinsically help in compensating charge unbalance and eventually enhance the structure stability by inducing at the same time oxygen and Ti vacancies. The N,Nb-codoping of titania has been recently discussed in a theoretical study investigating its photoelectrochemical properties.[24] On the experimental side, Breault and Bartlett[36-37] discussed heavily doped $TiO_2$ systems (defined by the authors as coalloys). They showed that very large amounts of dopants (Nb contents up to 30%) imply changes in the band edges that result in overall lower band gap materials. Keller *et al.*[18] prepared N,Nb codoped titania nanotube arrays which show relevant visible light photoelectrochemical activity due to contents up to 15% of Nb in the near-surface region. The only work relative to a conventionally N, Nb codoped $TiO_2$ system is, to the best of our knowledge, the one by Lim *et al.*[38]. In this case the samples, prepared by a sol-gel procedure with $0.001 < Nb/Ti$ molar ratio $< 0.03$, show N-Nb synergistic photocatalytic effects with respect to both the oxidation and the reduction of water pollutants.

In few words, the combination of Nb and N appears to be a novel and promising doping strategy to enhance the photoactivity of titania-based materials. However, the reasons underlying this evidence are still far from being fully understood. In this work, we aim at bridging this gap. A possible electronic mechanism, where bulk Nb and N dopants cooperate synergistically, is proposed to account for experimental results. The compensating model for Nb/N titania codoping described above has already been put forward[24] but it has never been substantiated by a broad and thorough series of theoretical and experimental characterizations proving Nb lattice location and valence. This study is motivated by the superior photocatalytic performance of the codoping with respect to each single doping solution.[38] More in detail, we synthesized a series of N, Nb nanocrystalline

titania samples, both mono- and codoped, by a sol-gel procedure in the low doping range that has shown more promising photocatalytic results.[38] Crystallographic structure, local structure, microstructure and morphology of the powders were then probed at various length scales (from $10^{-10}$ to $10^{-6}$ m) by means of several experimental approaches. At the same time, measurements providing information on the corresponding optical properties and defective features were performed. Finally, periodic plane-wave DFT calculations were performed to supply a solid interpretative basis of the whole picture, explaining how different guest species and intrinsic point defects cooperate in determining the observed experimental response. Although the final application of presented materials is photocatalysis, a detailed investigation of the photocatalytic performance is out of the scope of the present report. The interested reader is therefore referred to previous studies presenting detailed reports of the photocatalytic performance of N,Nb-codoped $TiO_2$.[37-38]

## 2. EXPERIMENTAL AND THEORETICAL METHODS

### 2.1 Nanopowder synthesis

All reactants were purchased from Sigma Aldrich and were used without further purification. Doubly distilled water passed through a Milli-Q apparatus was used. Titania samples were prepared by a sol–gel synthesis using the following procedure. Titanium (IV) isopropoxide was dissolved in 2-propanol, using a molar ratio 1:5. Then, an aqueous solution of HCl was added drop-wise under vigorous stirring (300 rpm), in order to obtain a $H_2O$ : titanium (IV) isopropoxide molar ratio of 100 and final pH 3. The slurry was stirred for 90 min to complete the hydrolysis. Then, the solvent was completely removed by drying in oven at 80 °C. The obtained powders were ground and calcined at 400°C for 6 h in either $O_2$ or $N_2$ flux (9 NL $h^{-1}$).

Nb-doped samples were obtained by adding $NbCl_5$ to the titanium (IV) isopropoxide solution, while Nb,N-codoped samples were synthesized using ammonium niobate(V) oxalate hydrate ($NH_4[NbO(C_2O_4)_2(H_2O)] \cdot n\ H_2O$) as a source of both N and Nb. This implies that codoped

samples always nominally contain an equimolar quantity of both the N and Nb guest species. Undoped and N-doped samples were also synthesized, the latter using $NH_4OH$ as precursor.

Samples will be denoted as TD1D2*x*, with D1 and D2 being the dopants and *x* the dopant/Ti nominal molar ratio (0.5-5%). 'T0' represents the undoped $TiO_2$ reference. A $N_2$ mark distinguishes the samples calcined in $N_2$ flux. Otherwise, it has to be intended that calcination was carried out in an $O_2$ atmosphere.

## 2.2. Materials characterization

*2.2.1 High-resolution X-ray powder diffraction (HR-XRPD).* HR-XRPD experiments were performed at the bending magnet BM01B station of the Swiss-Norwegian beamline at the European Synchrotron Radiation Facility (ESRF), in Grenoble, France. Data were collected from 4° to 50° in $2\vartheta$ at 0.9 °/min in Debye-Scherrer capillary geometry using Si (111)-monochromated X-rays with $\lambda$ = 0.50494(3) Å. The Rietveld method as implemented in the GSAS-EXPGUI program suite[39-40] was utilized to fit experimental diffractograms. The Williamson-Hall method was applied to integral breadths of individual *h0l* reflections up to $\sin\vartheta/\lambda$ = 0.5 $Å^{-1}$ to estimate the average volume-weighted crystallite dimensions, $\langle D_v \rangle$. More details on the HR-XRPD experiments and information on the statistical agreement factors of the fitting (Table S1 SI) can be found in the Supporting Information (Section S1 SI).

*2.2.2 Extended X-ray Absorption Fine Structure (EXAFS).* Thin tablets suitable for recording X-ray absorption spectra were prepared by pressing powder specimens. Samples intended for measurements at the Ti K edge were also carefully diluted in cellulose to avoid thickness effects. X-ray absorption curves were then collected around both Ti K and Nb K edges at room temperature at the BM01B beamline of ESRF. Ti spectra were recorded in transmission mode, while for Nb we had to resort to fluorescence mode as the signal in transmission geometry was partly contaminated by a spurious Bragg reflection due to the crystal monochromator. A Si (111)-monochromated beam was

employed to probe the nanostructured samples in the 4.88 – 6.00 (Ti K edge) and 18.9 – 20.0 keV (Nb K edge) energy ranges. The Horae suite of programs[41], based on the IFEFFIT library[42], was used throughout data processing and fitting. The same multi-step fitting strategy described in detail elsewhere[43] was applied to extract information on the average coordination geometry around Ti. As for the spectra at the Nb K-edge, we considered as negligible the amount of dopant possibly present in the minority phase of brookite with respect to the major anatase one. Therefore, just the backscattering paths due to the anatase lattice were taken into account to model the average first and second coordination shells of the guest transition metal. Information on the parameter statistics and agreement factors, together with full details on the fitting procedure, can be found in the Supporting Information (Section S6).

*2.2.3 Electron Paramagnetic Resonance (EPR).* EPR spectra were measured at room temperature and at 77 K using an X-band EPR spectrometer (Bruker Elexsys) at the working frequency of 9.4 GHz. The Bruker SimFonia program was used to perform the spectral simulations.

*2.2.4 Specific surface area and porosity determinations*. The sample specific surface areas were determined by the Brunauer-Emmett-Teller (BET) procedure using a Coulter SA 3100 apparatus. The pore size distribution was determined from the desorption isotherms using the Barrett-Joyner-Halander (BJH) method.

*2.2.5 Electron microscopy*. The sample morphology and elemental composition were determined by a scanning electron microscope (SEM, Zeiss LEO 1430) working at 30 keV, equipped with a backscattered electron detector and an energy dispersive X-ray analysis (EDX) system.

*2.2.6 Diffuse reflectance spectroscopy (DRS).* The optical properties of the powders were determined by DRS using a Lambda 35 UV-vis spectrophotometer (PerkinElmer) equipped with an integrating sphere. The apparent band gap values were determined using the Kubelka-Munk equation.[9]

### 2.3. DFT modeling

We performed spin-polarized calculations with VASP suite of codes[44-49] The projector augmented wave (PAW) pseudopotentials were employed[44-45] and the Perdew-Burke-Ernzerhof parametrization[48] was utilized in generalized gradient approximation[50] for the exchange-correlation potential. The energy basis cutoff was 400 eV and the optimizations were performed using the conjugate-gradient scheme[51-52] until the change in total energy between successive steps was less than 0.001 eV and residual forces were below 0.01 eV/Å. For Nb doping, agreement with experimental results was obtained using corrections for the self-interaction errors, such as the DFT+U approach[53]. An effective on-site Coulombic interaction correction U (U=U'-J) was employed for the Ti 3d orbitals. The value of U=3.3 eV was used because it has previously been shown to properly account for the electronic structure of the Ti 3d states.[54-57] The reciprocal space was limited to the single Gamma point, given the 3x3x3 primitive supercell arrangement.

## 3. RESULTS AND DISCUSSION

The chemical composition of the samples was investigated by EDX analysis. The experimental Nb/Ti molar ratios are slightly lower than the calculated nominal ratios (Table S2 SI), as commonly reported in the literature[37]. The nitrogen content needs instead a more detailed discussion. The very low N/Ti ratios present in these samples cannot be verified by EDX due to experimental limits and also to a partial overlap of N and Ti spectral lines. Indeed, previous studies have shown that the actual nitrogen content in $TiO_2$ lattice is generally much lower than the nominal amount, since an appreciable loss of N containing species occurs during calcination.[11, 14] Nitrogen bulk quantification is quite a challenging task, since conventionally used techniques, such as X-ray photoelectron spectroscopy (XPS), provide information about the surface and near-subsurface composition of the oxide, which is greatly influenced by the presence of atmospheric contaminants

(C, N and O).[8] Previous studies on Nb-doped $TiO_2$ have also underlined other relevant discrepancies between bulk and surface compositions in such systems, such as a higher Nb content at the surface due to the occurrence of surface segregation phenomena[58]. Further, Bartlett and coauthors[36] reported by XPS the absence of any $Ti^{3+}$ in heavily N,Nb-codoped samples, which was instead detected by EPR analyses. Being interested in the bulk effects of doping and codoping, we have chosen to rely on characterization techniques that are not merely surface sensitive, such EDX and EPR, to probe the composition and defective state of our samples.

### 3.1 Microstructure

*3.1.1. Phase composition.* Figure 1 shows the least squares fitting results *vs.* the observed diffraction intensities for the undoped T0 specimen and for a series of mono- and codoped nanopowders. Small fitting residuals are present in the diffractograms. These are due to the small inaccuracies of the final least-squares structural model in the description of profile asymmetry caused by axial beam divergence affecting low-order reflections. Also the highly defective nature of the nanostructured powders (see *infra*) implies small anisotropies in the line profile broadening at higher angles. Nevertheless, the residuals are well-centered around the peaks and they average to zero, *i.e.*, cell parameters and main peak intensities are satisfactorily matched (see Table S1 SI for the statistical fitting parameters).

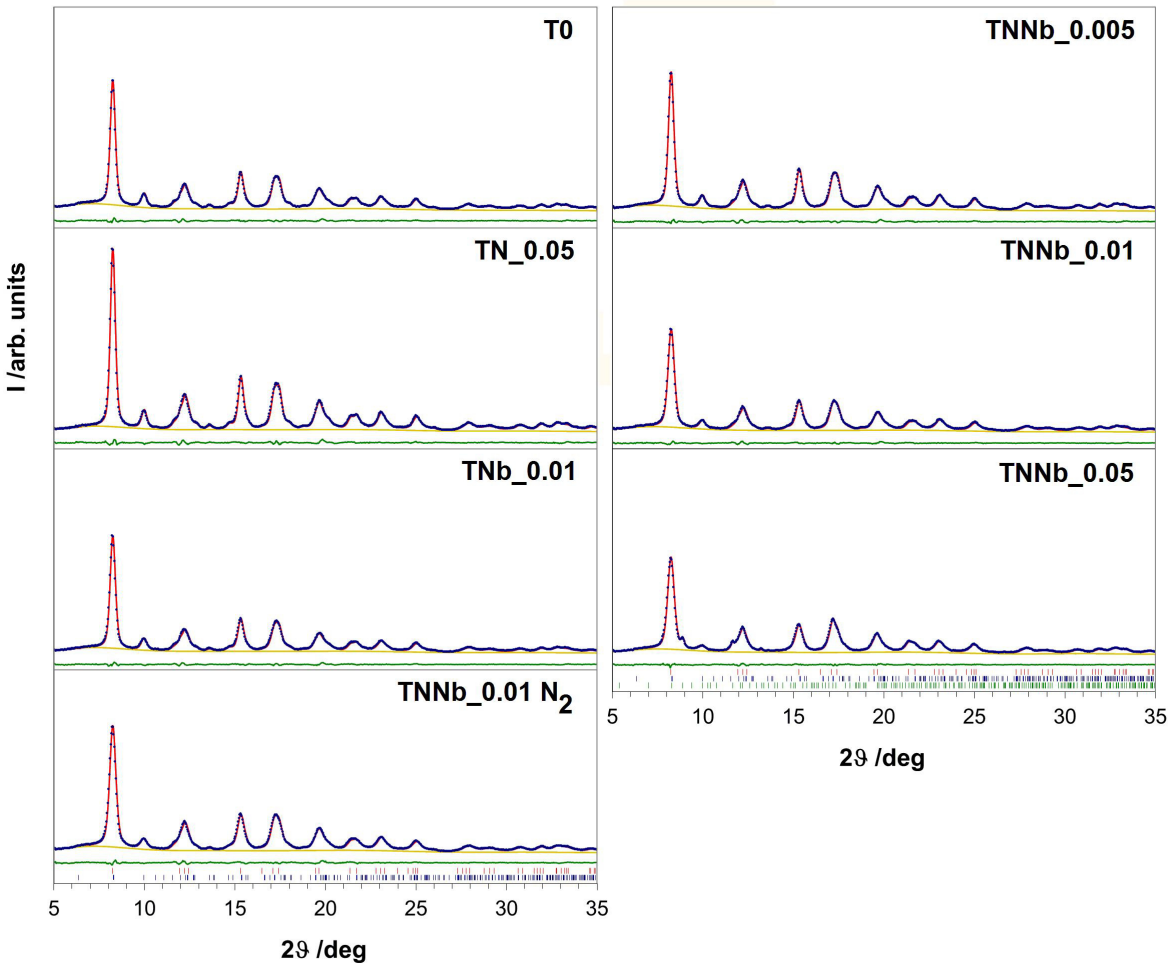


**Figure 1**. Color online. Collected powder patterns (blue dots). The least-square fitting curves are in red, the $y_{obs}$-$y_{calc}$ point-by-point difference in green and the refined background function in yellow. Intensities are drawn on a common arbitrary scale. The diffractions for the anatase, brookite, and $NbO_2$ phases are shown as red, blue and green markers, respectively.

As we expected on the basis of our previous experience on similar materials[8, 11, 43], the major phase component is always $TiO_2$-anatase (space group: $I4_1/amd$) with a non-negligible minority of brookite (*Pbca*), as it can be inferred from the peak at $2\vartheta \approx 10.0^{\circ}$ originated from the (211) reflection of this phase. The most heavily codoped specimen (TNNb_0.05) shows in addition a small amount (≈ 5%, Table S3 SI) of segregated α-$NbO_2$ oxide ($I4_1/a$)[59]. The segregation is clearly appreciable in the diffractogram from the secondary peak at $2\vartheta \approx 8.9^{\circ}$, which are attributable to

(400) and (040) equivalent reflections of the contaminating Nb oxide. Apart from α-$NbO_2$ oxide, no other crystalline phases were detected in our samples, since any attempt to add other Nb-containing structures to the model invariably led to the worsening of the least-squares fitting. The occurrence of surface segregation of $Nb_xO_y$ is often reported at high Nb loadings[58, 60-61], although the Nb content which determines such an effect and the obtained crystalline/amorphous phases strictly depend on the adopted synthetic conditions (e.g., type of Nb precursor, calcination conditions, synthetic approach). The α-$NbO_2$ phase observed in the TNb_0.05 sample appears as a highly crystallographic strained phase on the grounds of the Williamson-Hall results (Table S5 SI).

More quantitative information on the phase composition of the nanostructured powders is appreciable in Figure 2, where the trend of the brookite content is shown as a function of the nominal doping extent. Interestingly, a single dopant species has a less appreciable effect on the brookite amount, that remains essentially unchanged (≈ 31%) on going from the undoped T0 reference material to the TNb_0.01 and TN_0.05 samples. On the contrary, the simultaneous presence of both N and Nb in the bulk structure invariably implies a significant decrease of the brookite phase, down to ≈ 14 % in the TNNb_0.05 material (green rhombi in Figure 2). It is known that inclusion of the N dopant alone has a similar effect on the phase composition[8-9], but the changes here observed occur at much lower dopant loadings. Moreover, the calcination conditions scarcely influence the final material composition, as the TNNb_0.01 samples bear an almost identical amount of brookite whether they are calcined in $O_2$ or $N_2$ (see the red triangle in Figure 2). All these evidences imply that the observed changes are neither due to specific synthetic conditions nor attributable to just one of the N, Nb guest species. Rather, the inclusion of *both* the dopants in the crystallographic structure should imply a strong thermodynamic driving force toward the formation of the anatase phase at the expense of brookite, as dopant-induced changes have appreciable effects even at very low loadings. Moreover, these evidences also suggest that guest species are most likely preferentially allocated into the anatase lattice.

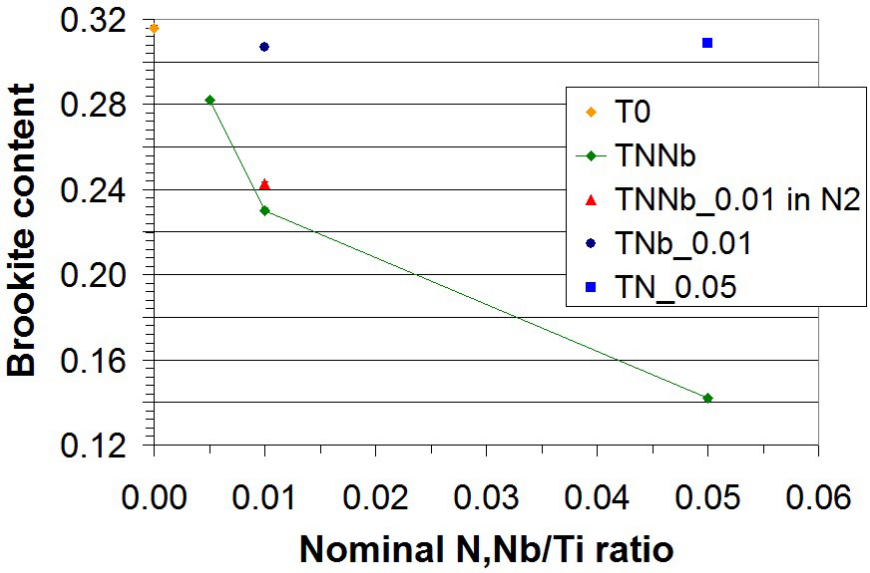


**Figure 2**. Color online. Brookite content as estimated from the Rietveld refinement of the HR-XRPD data. The green line guides the eye and highlights the codoped N,Nb series of materials. The diameter of the dots roughly corresponds to 1 estimated standard deviation (e.s.d.).

*3.1.2. Crystallite dimensions*. The volume-weighted average crystallite sizes, $\langle D_v \rangle$, of the two phases are quite similar (Figure 3, Table S5 SI). The presence of a single N or Nb dopant species does not affect $\langle D_v \rangle$ at all, that remains constant at ≈ 45 Å as in the bare T0 phase. On the contrary, both phases show a general tendency toward producing smaller crystallites when both N and Nb are introduced, even though changes in anatase are more pronounced than in brookite. The only exception is TNNb_0.01 $N_2$ (red triangle in Figure 3b), in which also the brookite phase is characterized by a significantly smaller crystallite average dimension than the $O_2$-treated analogue.

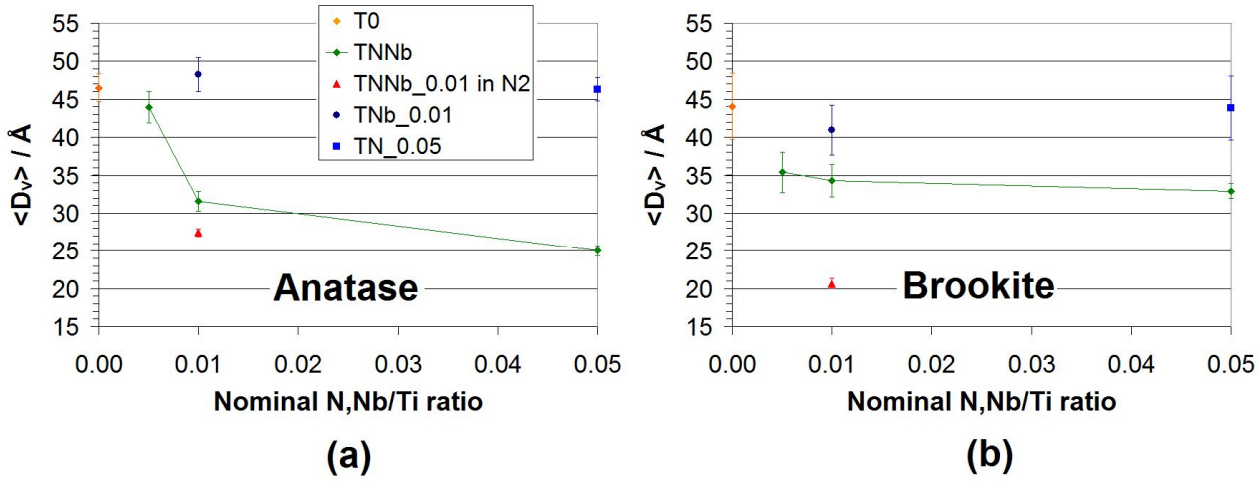


**Figure 3.** Color online. Average volume-weighted crystallite dimensions of anatase (a) and brookite (b) phases as a function of the nominal doping extent. The reported values have been computed from integral breadths of *h0l* reflections up to $2\vartheta = 30°$ by means of the Williamson-Hall method. Error bars correspond to 1 e.s.d.

It is worth comparing the structural properties of the present series of codoped samples with previous results on N-doped samples[8], which exhibited in this respect an opposite behavior. While the concomitant addition of N and Nb results in both an increase of the anatase content and a drop of its average crystallite dimension, N-doped materials showed an increase of both the anatase content and of the crystallite size at increasing (> 0.2) N/Ti nominal molar ratios[8]. A possible explanation of this contrasting behavior might be related to the nucleation and growth kinetics of the crystallization process. The observed codoping-induced strong thermodynamic bias toward anatase implies a large and negative free energy change associated to the appearing of the $I4_1/amd$ phase. The bias is larger when N and Nb concentration is increased. According to this scenario, the critical radii of anatase nuclei should become smaller[62] at increasing (N+Nb)/Ti molar ratios, assuming that the surface tension associated to the habit of anatase crystals does not change in bulk-doped samples with respect to the T0 reference. Therefore, we believe that nucleation should be faster in the codoped case than in single-doped $TiO_2$:N materials and the crystallite average

dimensions smaller as the N,Nb loading is raised.

*3.1.3. Morphological features.* Figure 4a reports the comparison among the adsorption isotherms of $N_2$, obtained in subcritical conditions, in the case of undoped $TiO_2$ and of the 1% doped samples, both mono- and codoped. All the samples show hysteresis loops characteristic of a mesoporosity.

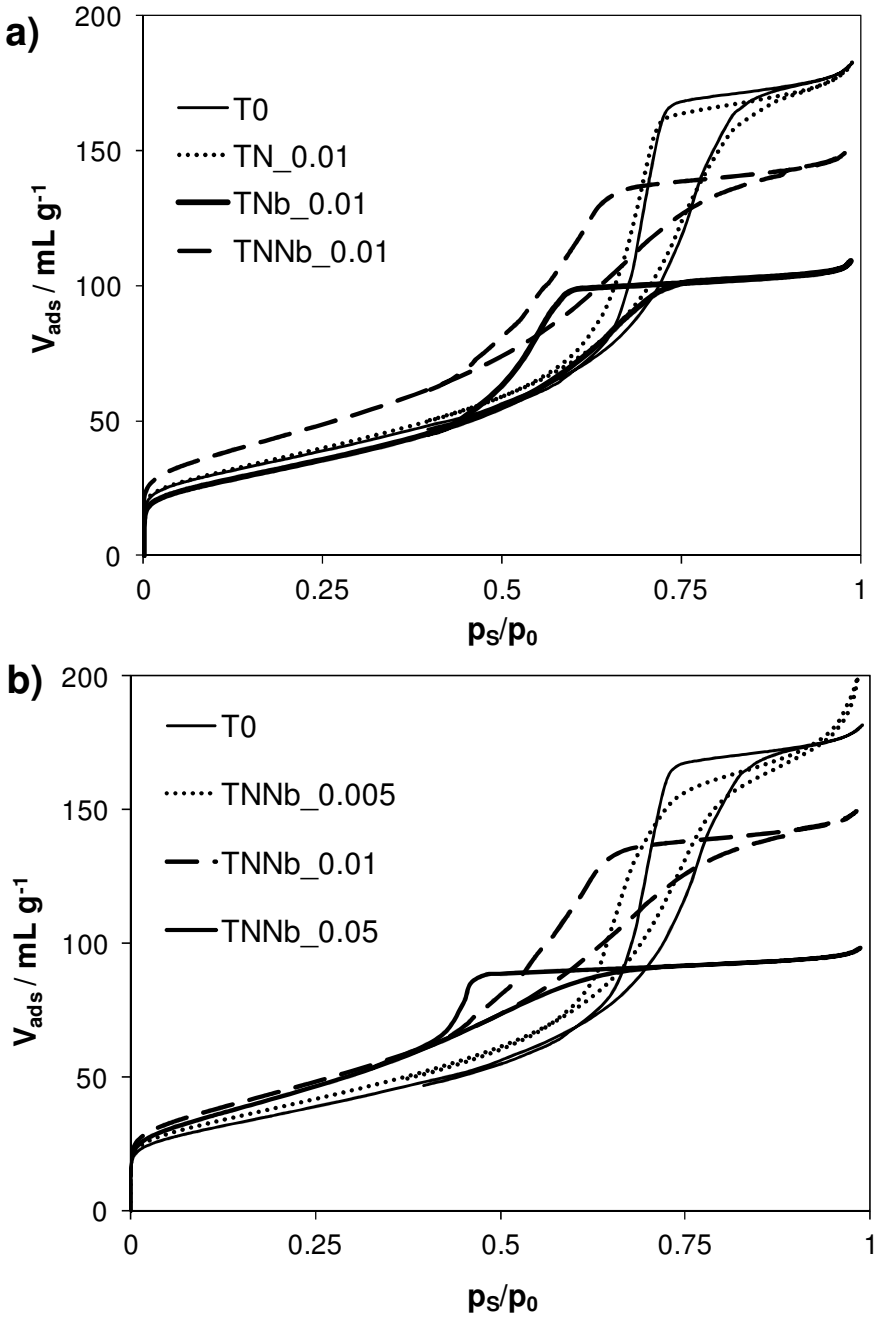


**Figure 4**. Adsorption isotherms of $N_2$, obtained in subcritical conditions, of the undoped and mono- and codoped samples, with the relative hysteresis loops. a) Comparison among undoped and 1%-

doped and codoped systems. b) Comparison among the different N,Nb-codoped samples.

In any case the presence of dopants induces a shift of the hysteresis loop to lower pressures indicating a decrease in the pore sizes, more so when Nb is present. The effect is even more conspicuous when higher Nb dopant contents are considered (Figure S2a SI). The effect of the sole N-doping seems almost negligible on the morphological features of $TiO_2$, even when higher dopant contents are considered (Figure S2b SI). The presence of the sole Nb induces a small decrease in surface area (Table 1) and a relevant decrease in the total pore volume (Figure S3 SI).

**Table 1**. Specific surface area ($S_{BET}$), total pore volume ($V_{pores}$) and apparent band gap ($E_g$) of the bare and doped samples.

| sample | $S_{BET}$ $m^2\ g^{-1}$ | $V_{pores}$ $mL\ g^{-1}$ | $E_g$ eV |
|---|---|---|---|
| *T0* | 129 | 0.293 | 3.16 |
| *TN_0.01* | 132 | 0.290 | 3.13 |
| *TN_0.05* | 123 | 0.293 | 3.09 |
| *TNb_0.01* | 119 | 0.166 | 3.04 |
| *TNb_0.05* | 113 | 0.097 | 2.96 |
| *TNNb_0.005* | 140 | 0.324 | 3.19 |
| *TNNb_0.01* | 161 | 0.223 | 3.11 |
| *TNNb_0.05* | 154 | 0.102 | 2.93 |
| *TNNb_0.01 $N_2$* | 166 | 0.256 | 3.09 |

The presence of both dopants (TNNb_0.01) has a different effect with respect to the two single dopants (Figure 4a). The codoping supports an appreciable increase in surface area (about 30% for both calcination atmospheres) while the total pore volume remains almost unchanged (Table 1).

With respect to the undoped sample (T0), the pore sizes of the two codoped samples decrease (Figure S3 SI). This latter occurrence, together with their lower crystallite sizes (Figure S4

SI), can be the origin of the observed increase in surface area for the codoped samples. The synergistic role played by the concomitant presence of both dopants is apparent also in the case of sample TNNb_0.05, which shows a larger surface area with respect to both undoped and single-doped samples (Figure S2 SI). Once more, this is the joint result of smaller crystallites (Figure S4 SI) and smaller pores (Figure S3 SI).

The comparison among the three codoped samples, (Figure 4b, and Table 1), shows that a progressive increase in surface area accompanies the parallel decrease in the crystallite sizes. In the case of TNNb_0.05 the relevant loss in pore volume partially smothers the surface area increase. It should be recalled that this sample shows also the occurrence, although to a limited extent, of $NbO_2$ segregation from the titania lattice.

SEM images (Figure S5 SI) show that samples present aggregates at the micrometer scale. No well-formed crystal facets are clearly recognizable. Rather, the powders are organized at the mesoscale as sintered grains made up by differently oriented crystallites. As for the series of codoped $TiO_2$:N,Nb, systems, the similar trend of the pore volume and the average crystallite dimensions suggests that most of the void space is due to inter-grain cavities and interstices.

### 3.2 Electronic structure

Bulk plane-wave DFT simulations are nowadays routinely employed to investigate the electronic properties of complex materials. DFT+U has proved to be appropriate to describe Nb anatase doping.[63-65] As for the present work, it is crucial to understand how the N and Nb codopants interact with each other and what is their cooperative effect, if any, on the predicted position of any gap state and the Fermi Energy in k-space. Experimental results (see Section 3.1) ensure that codoping has a significant effect on the material microstructure. Thus, a comprehensive investigation of the electronic structure as a function of the doping scenario is mandatory to correlate the observed enhanced visible light absorption (see the following, Section 3.6) to

compositional, crystallographic and morphological degrees of freedom. To this end, we chose to restrict our investigation to the anatase phase, as (i) diffraction experiments demonstrated that anatase is the prevailing phase in all the samples, and (ii) the brookite content diminishes as the N, Nb loading increases.

Our first-principle simulations show that Nb ions pull the Fermi Energy (FE) toward the conduction band (CB, Figure S6 SI and Table S6 SI). It is worth noting that this is true for both interstitial and substitutional metal dopants, as electron-donor Nb species invariably create high-energy partially filled states in the CB proximity. In other words, Nb 4d orbitals mix well with Ti 3d ones and the excess electron formally reduces a Ti site to $Ti^{3+}$.[63-68]

The picture becomes quite different when both N and Nb are simultaneously added to the anatase lattice (Figure 5). As already calculated for N doping[9, 69], valence nitrogen states lie in the proximity of the valence band (VB). When Nb is placed as interstitial ($Nb_i$), the two guest species are electronically uncorrelated and the position of FE is again determined just by the shallow CB Nb states (Figures 5c-d). Instead, when substitutional Nb is considered ($Nb_s$), an electron transfer to low-lying partially filled N states takes place and empties the Nb CB states . In the case of the interstitial Nb doping, there are more shallow CB states and any eventual electron transfer does not empty all of them. As a consequence, the FE abruptly shifts toward the VB (Figure 5a,b and e) only when the Nb doping is substitutive. This behavior implies that partial intrinsic charge compensation occurs when Nb goes in substitutional position. These conclusions are completely general and as a result, codoping with substitutional Nb is advantageous with respect to mono-doping since the semiconductor characteristics are preserved thanks to charge balance[66]. In particular, they hold true independently of the location of the nitrogen atom (interstitial or substitutional). It is also important to stress that no defect clustering has been forced during the simulation, as no point defects were placed as close neighbors within starting unit cell geometries.

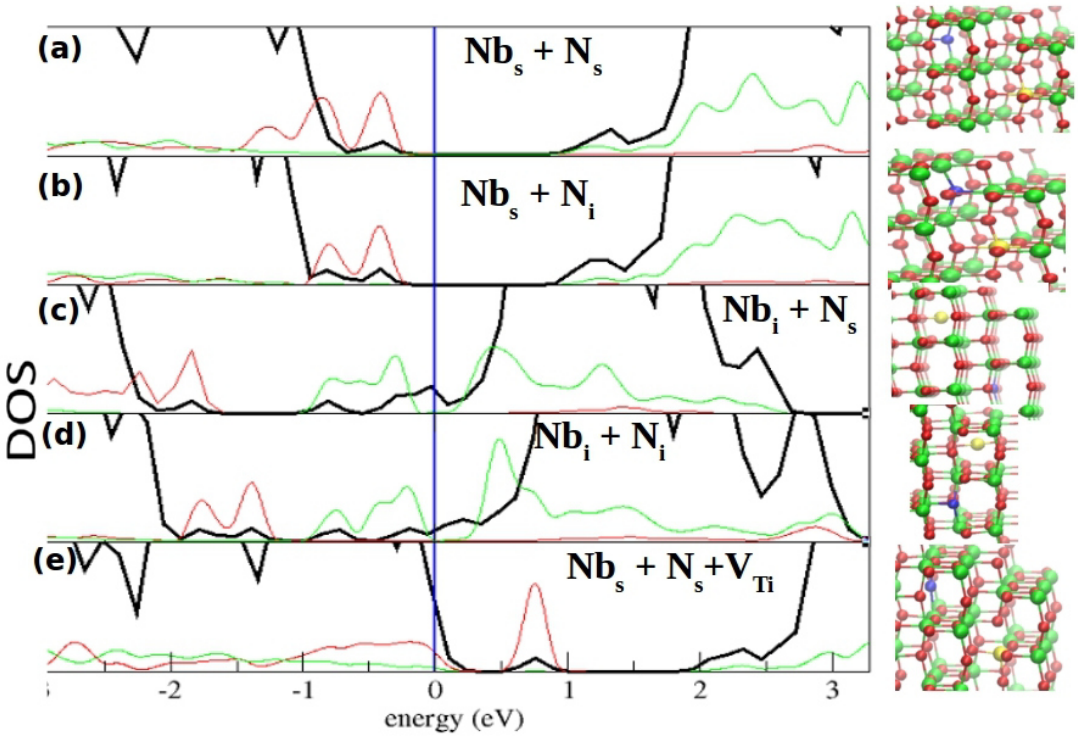


**Figure 5.** Color online. Computed density of states (DOS) of $TiO_2$-anatase for different doping scenarios (Nb,N,$V_{Ti}$/Ti = 1/54): a) ….. Black curve: Total DOS. Red curve: Magnified partial DOS, projected on N atoms. Green curve: Magnified partial DOS, projected on Nb atoms. 's' and 'i' subscripts describe the point defect type and stand for 'substitutional' and 'interstitial' species. Insets: local geometries. Green atoms for Ti, red for O, blue for N, yellow for Nb. The Fermi Energy (FE) is marked as a vertical blue line.

When an oxygen vacancy is included in the simulation of the codoped lattice, the empty $Ti^{3+}$ states near the CB become populated due to the electrons released to maintain charge neutrality. Therefore, FE invariably shifts toward CB, no matter the location of the guest species (see $Nb_x + N_y + V_O$ entries in Table S6 SI, with *x*, *y* being either 's' or 'i'). Despite this apparent similarity, it should be stressed that the two doping models imply important differences, as the intrinsic Nb-N charge compensation is expected to occur in the $Nb_s$ case, but not in the $Nb_i$ one.

The lower panel of Figure 5 shows the effect of Ti vacancies on a $N_s + Nb_s$ codoping scenario. The Ti vacancies shift the Fermi level toward the VB edge and populate the N electronic

levels.

Considering the differences in the charge compensation phenomena, either model ($Nb_s$, $Nb_i$) might imply a different mechanism through which the material will interact with UV-Vis photons. As a result, we can speculate that electrons transferred from Nb substitutional into intra-gap N levels can act as visible photoexcited carriers. As a consequence the visible light absorption performance is expected to be improved. Therefore, understanding the actual nature (interstitial or substitutional) of Nb dopants is crucial to provide a solid interpretative basis for the experimental results. A possible strategy to achieve this goal consists in investigating the local coordination geometries around Nb metal centers.

### 3.3. Nature of point defects

No significant changes were detected in the Ti coordination geometry from Ti K-edge EXAFS spectra throughout the sample series, as expected from the very low dopant content. The interested reader can find a detailed discussion on this topic in the SI (Section S6). In the following discussion, we will focus on the average geometry around Nb dopants to find correlations among their local chemical environment and the simulated structural and electronic properties of the material described above.

Direct- and k-space fitting results for the Nb K-edge EXAFS data can be found in Figure 6. The statistical fitting parameters are reported in Table 9 SI.

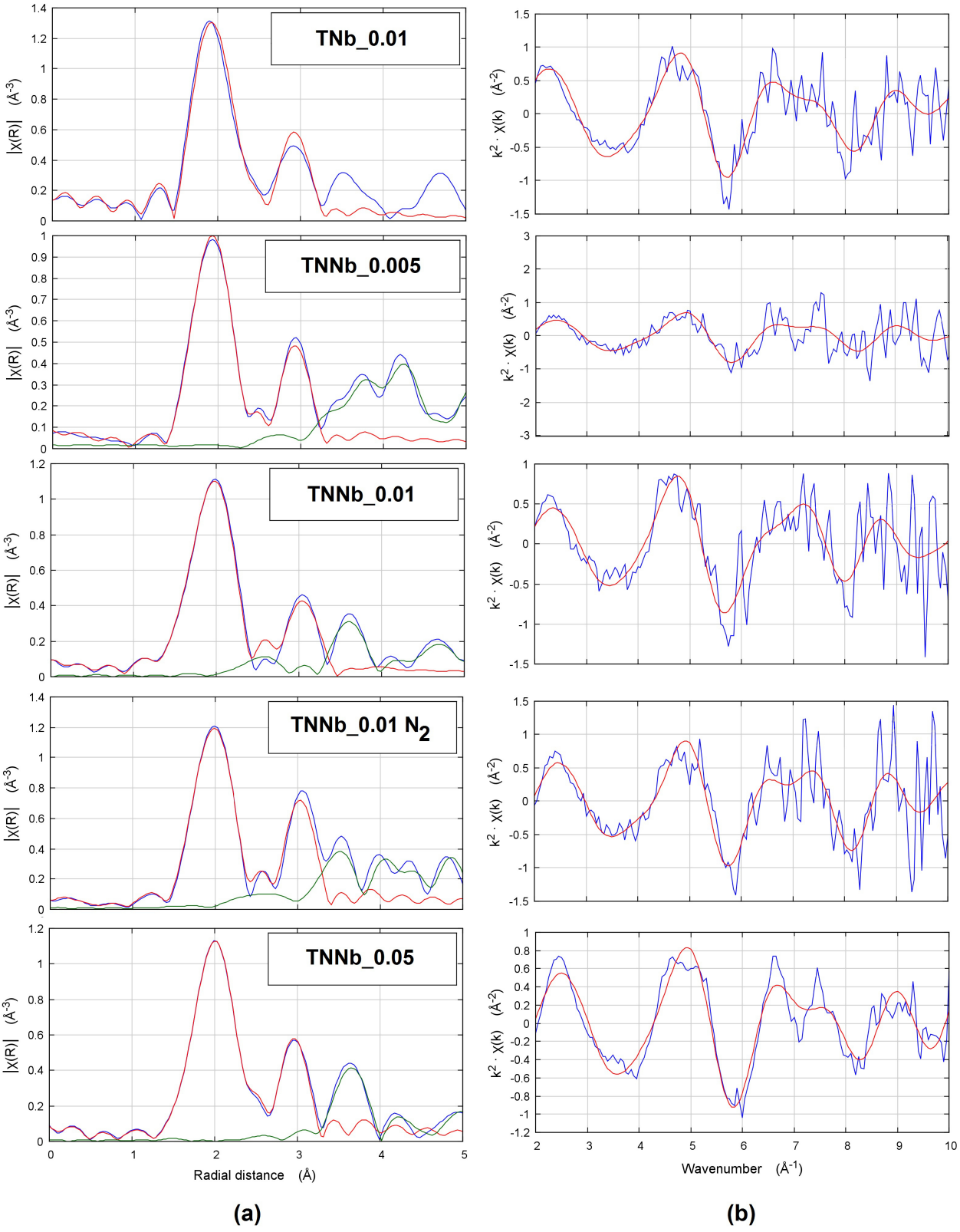


**Figure 6**. Color online. Fitted magnitude of the forward EXAFS Fourier transform (left) and corresponding fitted $k^2$-weighted Nb K-edge EXAFS spectra (right) of Nb-doped and N,Nb-codoped $TiO_2$ samples as a function of the doping extent. R-space curves were corrected for phase

shift. Blue curves: Experimental data; red curves: Least-squares fitting; green curves: Fitting residuals.

Table 2 compares the distances between Nb and its first and second nearest-neighbors as retrieved from DFT-optimized geometries and EXAFS fittings. For the sake of comparison, the crystallographic axial and equatorial Ti-O distances in the $TiO_6$ octahedra, as computed from the Rietveld refinement of T0 diffraction data, are 1.994(2) Å and 1.9298(4) Å, while the shortest Ti-Ti distance is 3.0310(2)Å. The same values as retrieved from high-resolution neutron diffraction data[70] are 1.9790(5) Å, 1.9340(1) Å and 3.0394(<1) Å, respectively.

**Table 2**. Comparison of the Nb-O and Nb-Ti phase-corrected distances as retrieved by EXAFS *vs.* those predicted by DFT+U PAW optimizations. Axial, equatorial and Ti-Ti distances calculated for undoped $TiO_2$ are reported as a reference. Values are expressed in Å. Estimated standard deviations of EXAFS results are given in parentheses.

| | $d_{Nb\text{-}O}$ axial | $d_{Nb\text{-}O}$ equatorial | $d_{Nb\text{-}Ti}$ |
|---|---|---|---|
| | | EXAFS | |
| TNb_0.01 | 2.0(2) | 2.0(1) | 3.03(1) |
| TNNb_0.005 | 2.0(2) | 1.98(8) | 3.03(1) |
| TNNb_0.01 | 2.0(8) | 2.0(4) | 3.15(1) |
| TNNb_0.01 $N_2$ | 2(1) | 2.0(7) | 3.11(1) |
| TNNb_0.05 | 2.04(2) | 1.96(1) | 3.02(1) |
| | | PAW-DFT [1] | |
| $Nb_s$ | 2.0398(3) | 1.969(1) | 3.1376(2) |
| $Nb_i$ | 2.026(1) | 2.128(1) | 2.6535(3) |
| $Nb_s+V_{Ti}$ [2] | 2.06(18) | 1.99(6) | 3.15(5) |
| | | DFT + U | |
| | $d_{Ti\text{-}O}$ axial | $d_{Ti\text{-}O}$ equatorial | $d_{Ti\text{-}Ti}$ |
| undoped $TiO_2$ | 2.007(2) | 1.9654(4) | 3.0698(3) |

[1] No crystallographic symmetry constraints were imposed while optimizing the geometry of the supercell. Therefore, slightly different distance values are predicted within each coordination shell. We report here average parameters, together with the corresponding standard deviations of the mean.
[2] A Ti vacancy was added to this structural model in the neighbor octahedron.

As expected, DFT+U calculations show that when Nb enters the anatase lattice, the oxygen first-neighbors are significantly displaced toward longer bond distances with respect to the reference crystallographic anatase structure[70] due to the greater effective ionic radius of the dopant ($Nb^{5+}$: 0.64 Å, 6-fold coordination) with respect to Ti ($Ti^{4+}$: 0.605 Å, 6-fold coordination)[71]. This is true when both interstitial and substitutional Nb atoms are considered (last rows of Table 2), even though DFT+U simulations predict greater equatorial $d_{Nb–O}$ estimates for the interstitial case. However, the most significant difference between the two scenarios ($Nb_s$ *vs.* $Nb_i$) resides in the second-shell distances. If Nb goes interstitial, a peak around 2.6 Å would be expected in the Fourier Transform of the fine structure function. Instead, if Nb goes in substitutional position, the 2$^{nd}$ shell Nb-Ti distances should fall around 3.0 Å. Indeed, this is just the case when the theoretical outcomes are compared with phase-corrected Nb-Ti coordination distances as retrieved by EXAFS spectroscopy (Table 2, first 5 rows and Figure 6a). Our results relative to both single Nb-doped and N,Nb-codoped $TiO_2$ are in agreement with EXAFS data reported by Bouchet and coauthors[72] in the case of single Nb-doped $TiO_2$.

Theoretical calculations predict a greater percentage increment of the Nb-Ti second-shell distance with respect to the Nb-O first-shell ones. This is due to the greater repulsion between $Nb^{5+}$ and $Ti^{4+}$ with respect to the $Ti^{4+}$ -$Ti^{4+}$ second neighbors in the undoped $TiO_2$. The first-shell oxygen atoms, in the case of Nb substitutional doping, are instead not as much affected since the greater attraction by $Nb^{5+}$ with respect to $Ti^{4+}$ is compensated by the greater Pauling radius of $Nb^{5+}$.

Unfortunately, the overall quality of the EXAFS fittings in terms of precision of the refined parameters is poor due to significant noise (see for example Figure 6b and Figure S9 SI). Nevertheless, the accuracy of the corresponding real-space refined parameters is satisfactory (Figure 6a) and the latter are in fair agreement with theoretical estimates for substitutional Nb.

It should be noted that EXAFS-derived results are also compatible with a doping scenario where a titanium vacancy, $V_{Ti}''''$, is added to the $Nb_s$ model. This has been proposed to be the expected scenario when the $TiO_2$-based phase is left free to equilibrate with high-activity $O_2$ species.[73] In the presence of this class of defects, PAW-DFT calculations predict, on average, statistically identical $d_{Ti-O}$ bond lengths for the axial and equatorial ligands (last row in Table 2). Interestingly, the same holds true for most experimental estimates, even though as the precision of the latter is generally too low, sound conclusions on this issue cannot be achieved.

Such a level of detail, however, can be reached by complementing information on the local coordination geometry available from EXAFS data with the long-range anisotropic strain affecting defective unit cells when the dopants are included in the lattice (Figure 7 and Figure S11 SI). The latter parameter can be computed from both HR-XPRD results and theoretical predictions, reported in details in Table S6 SI. In general, lattice microstrain is defined as the elastic distortion of the unit cell with respect to an unstrained reference lattice. Operatively, to single out the position of N and Nb dopants, we employ a strain parameter $\varepsilon_e = (l_e - l_{e0})/l_{e0}$, where $l_e$ is the length of a symmetry-independent crystallographic cell edge ($a$ or $c$), and $l_{e0}$ has the same meaning in a suitable reference crystal structure without dopants included. The unit cell retrieved in the undoped T0 material and the PAW fully relaxed anatase lattice were chosen as references for the HR-XRPD and DFT methods, respectively. According to the expected highly defective nature of the nanoparticles, DFT simulations always also took into account a single oxygen or titanium vacancy within the simulated lattice. If the microstrain along $c$, $\varepsilon_c$, is mapped against that along $a$ or $b$, $\varepsilon_{a,b}$, a two-dimensional diagram is obtained that allows to disentangle the relative effect of individual point defects on anisotropic structural distortions (Figure 7 and Figure S11 SI). When the cell edge distortions are due to interstitial Nb for mono- and codoped $TiO_2$, they invariably fall into the upper-left part of the diagram ($\varepsilon_c > 0.005$), whereas the distortions associated to substitutional Nb are significantly lower in magnitude. The presence of titanium vacancies further amplifies this trend, with $Nb_i$ models showing

a considerable (up to ≈ 0.009) strain along *c* no matter the nature (substitutional or interstitial) of the codopant nitrogen. On the other hand, very good agreement is found with the $Nb_s + N_s + V_{Ti}$ model and most experimental estimates, as the latter always show small strain parameters (< 0.002, 0.001) for both the *a* and *c* symmetry-independent crystallographic directions. In any case, the very small distortions with respect to the dopant-free T0 material are clearly incompatible with the massive presence of interstitial Nb ions.

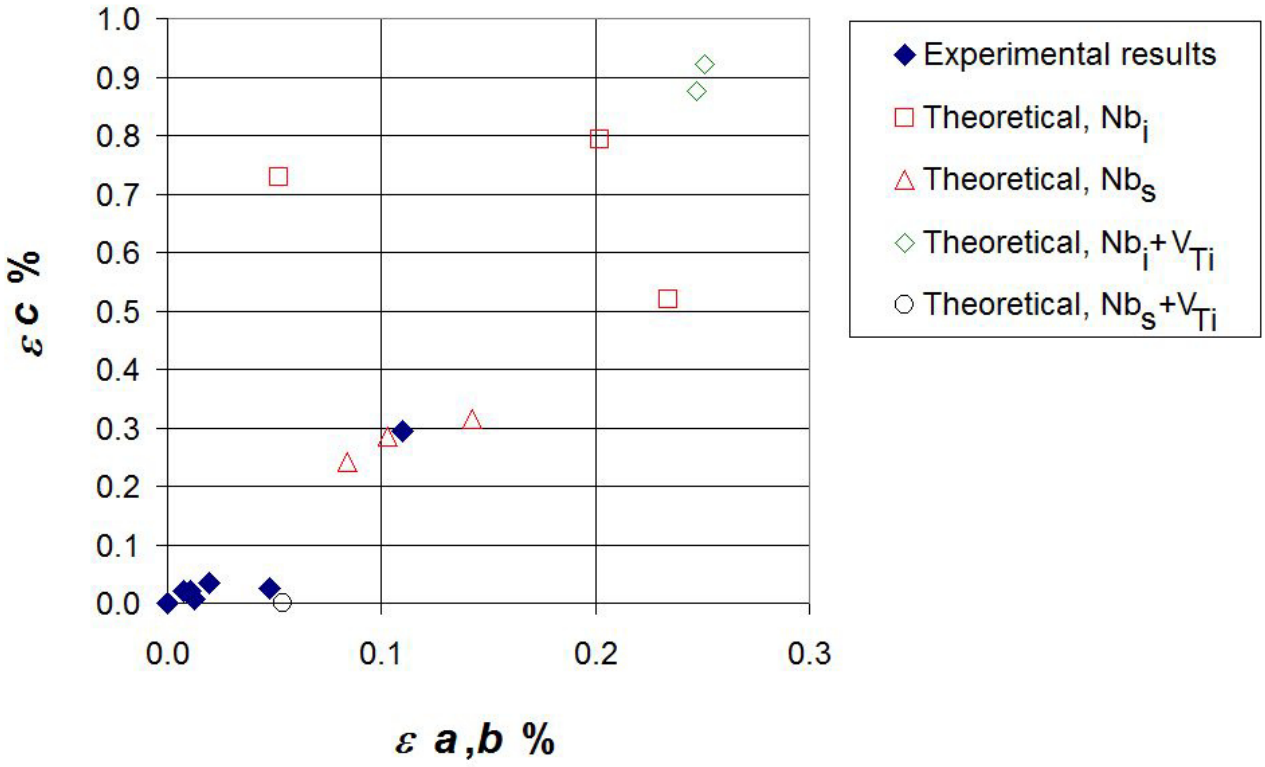


**Figure 7.** Color online. Anisotropic cell strain of Nb-doped and N,Nb-codoped samples as estimated by HR-XRPD and DFT+U methods with respect to the reference undoped anatase structure. Full rhombi: experimental results, as a function of Nb / N loadings (T0 is reported at the origin). Empty squares: DFT+U results, interstitial Nb. Empty triangles: DFT+U results, substitutional Nb. Details of the different theoretical models, together with labels of individual experimental results, can be found in Figure S11 SI.

In conclusion, both the EXAFS and HR-XRPD results, when compared with the outcomes of first-principle simulations, provide compelling evidence that Nb enters in substitutional position within the materials here considered.

### 3.5 Analysis of paramagnetic centers

The undoped T0 sample is EPR silent at both room temperature and 77 K. On the contrary, when dopants are introduced, the 77 K spectra show several features (Figure 8).

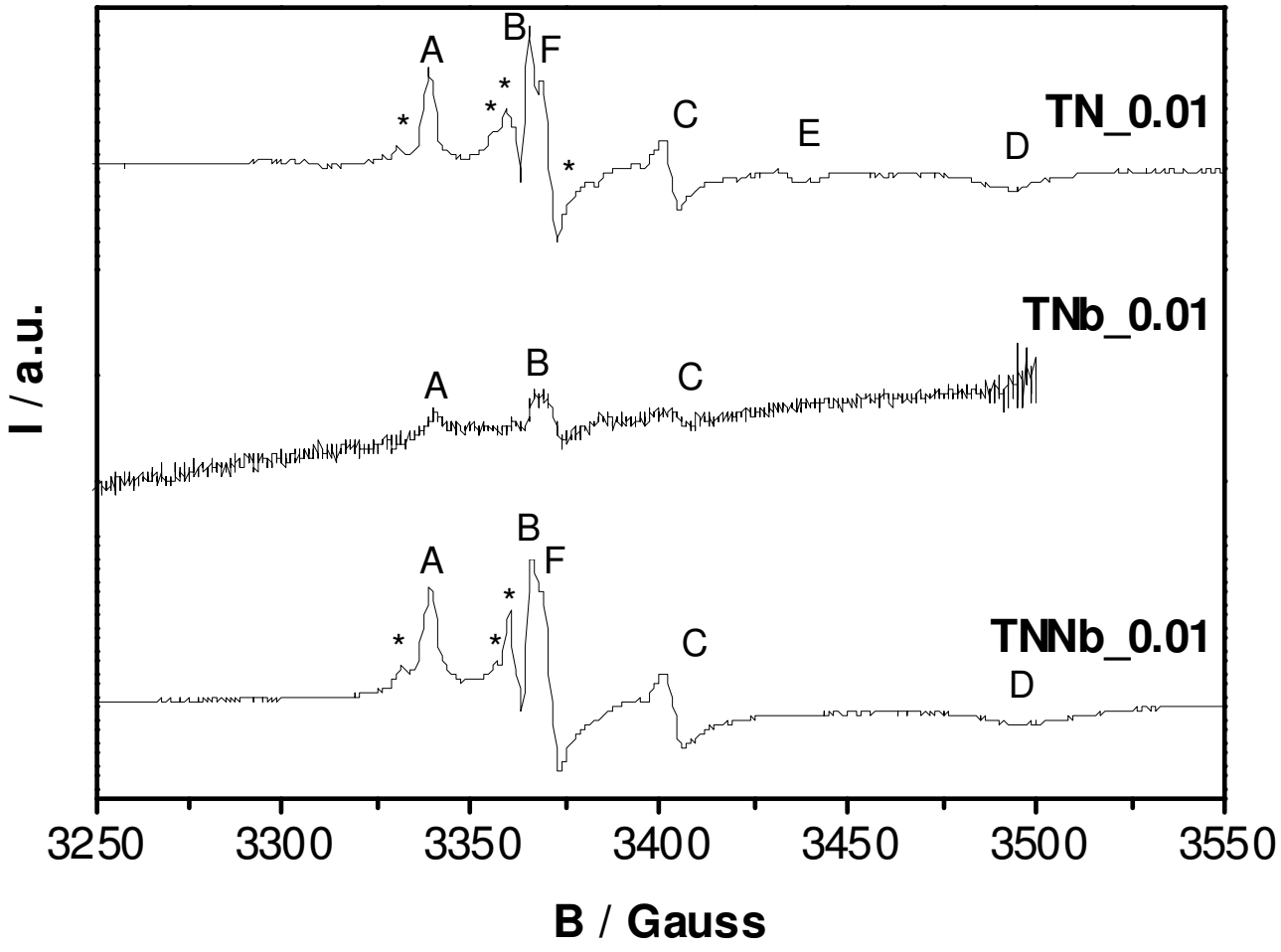


**Figure 8.** Experimental EPR spectra collected at 77 K of TN_0.01, TNb_0.01 (multiplication factor: 3.6) and TNNb_0.01 (multiplication factor: 0.78).

The TN_0.01 sample shows four narrow lines labeled by a star (*) in Figure 8. These features ($g_x$ = 2.066, $g_y$ = 2.0054, $g_z$ = 2.0040, $A_x \cong A_y \cong$ 3 G, $A_z \cong$ 32.2 G), which are appreciable even at room temperature, have been already reported elsewhere[10, 14] and attributed to bulk nitrogen paramagnetic defects ($N_b^{\bullet}$). Further, six other lines can be detected at 77 K, labeled in Figure 8 as A, B, C,D, E and F. The features A and B ($g_x$ = 2.0082, $g_y$ = 2.0118, $g_z$ = 2.0285) might be related to paramagnetic radical oxygen species[10, 74], while the lines C ($g_1$ = 1.98), D ($g_2$ = 1.93) and E ($g_3$ = 1.96) can be attributed to $Ti^{3+}$ in different environments, analogously to what was reported by the Giamello and coauthors[58, 75]. The attribution of C, D and E lines to $Ti^{3+}$ species is also supported by the fact that they cannot be detected at room temperature. Indeed, De Trizio *et al.*[61] reported that $Ti^{3+}$ signals cannot be observed above 100 K due to the occurrence of carrier detrapping at elevated temperatures.

At last, the F line is characterized by an intensity comparable to that of the B line, and can be simulated by a symmetric line with g ~ 2, attributable to $F^+$ paramagnetic defects, *i.e.* to almost free electrons trapped into oxygen vacancies. Previous studies reported the occurrence of $F^+$ defects in N-doped $TiO_2$.[14, 36]

The TNb_0.01 sample (Figure 8) shows a much less intense EPR spectrum, in which only the A, B and C peaks can be appreciated. Therefore, only oxygen radical and $Ti^{3+}$ species are appreciable in the Nb-doped sample. Several authors reported the occurrence of bulk $Ti^{3+}$ species in Nb-doped $TiO_2$ [58, 61, 75], whose formation was attributed to a mechanism of valence induction. Our results therefore support the occurrence of the valence induction mechanism for at least a fraction of the excess electrons introduced by the Nb dopant, although it is not possible, on the basis EPR data, to confirm or exclude the occurrence of the charge compensation mechanism of $Nb^{5+}$ involving titanium vacancies. Our DFT calculations support the hypothesis of $Ti^{3+}$ formation in Nb-doped $TiO_2$ (Section 3.2), although EXAFS-derived results are also compatible with a doping scenario where titanium vacancies, $V_{Ti}''''$, are present.

In the N,Nb-codoped sample (TNNb_0.01, Figure 8), the most striking difference with respect to the TN_0.01 is that the E line, shown by the N-doped sample and attributed to $Ti^{3+}$ ions, disappears in the N,Nb-codoped sample. The same comparison but at a higher dopant concentration (5%) is reported in Figure 9 and it clearly shows that in the N,Nb-codoped sample (TNNb_0.05) the $N_b^{\bullet}$ pattern becomes by far less intense than the AB pattern and the C, D and E features decrease or completely disappear.

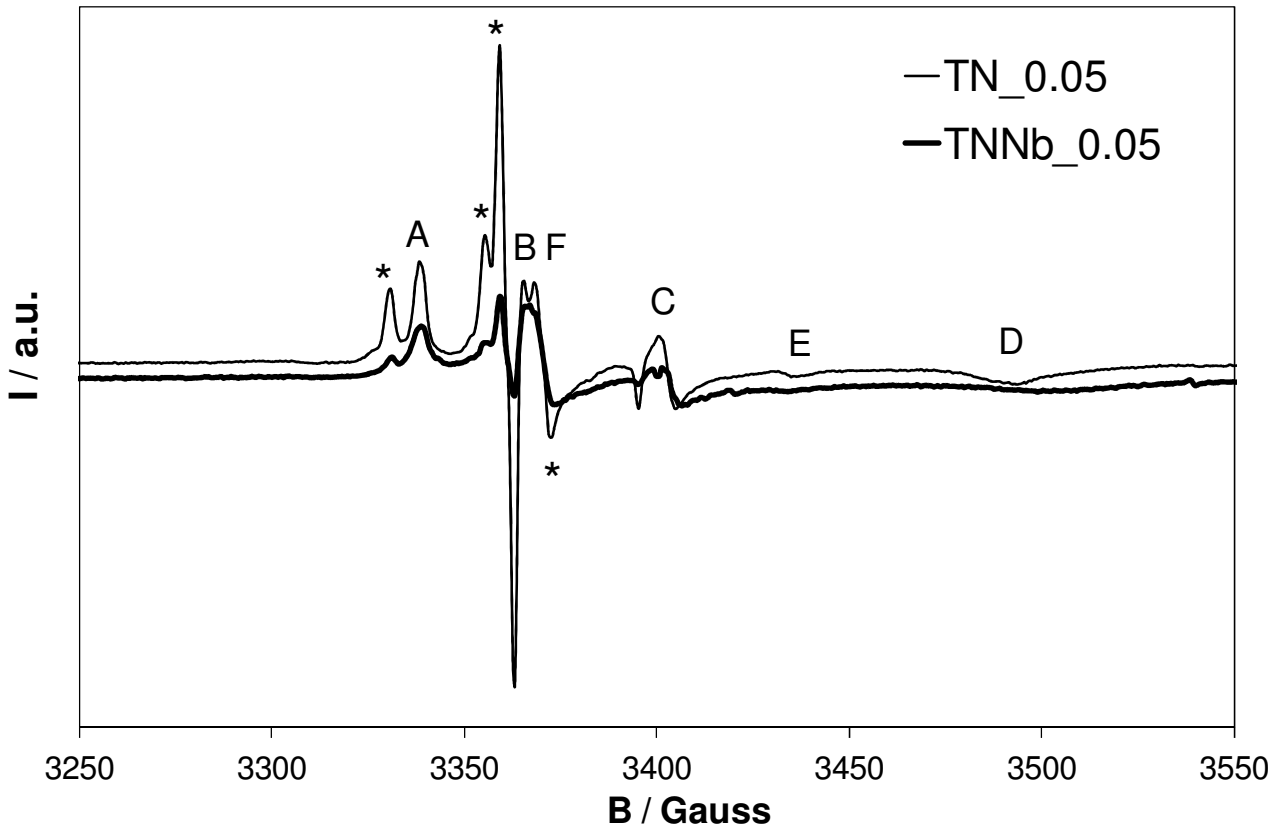


**Figure 9.** Experimental EPR spectra collected at 77 K of TN_0.05 and TNNb_0.05.

Both observations (disappearance of $Ti^{3+}$ and of N paramagnetic species in codoped samples) support the occurrence of charge compensation between Nb (acting as an electron donor) and N (acting as an electron acceptor) in the case of N,Nb-codoped samples, as predicted by our first-

principle DFT calculations in the case of substitutional Nb doping. This latter evidence further confirms the hypothesis of substitutional Nb doping in our codoped samples. However, the EPR spectra clearly show that such charge compensation phenomena are not complete, in agreement with previous reports by Bartlett and coauthors[36-37].

Figure S12 SI reports the comparison of three N,Nb-codoped samples with different nominal dopant contents (0.5-1-5%). As above mentioned, the E line is absent from the EPR spectra of all the codoped samples. We must outline that at high doping levels $NbO_2$ segregation can occur, as determined in the case of the TNNb_0.05 sample from XRD data. In this respect, it should be pointed out that TNNb_0.05 is the only sample showing a splitting of the C line, which might be related to the presence of $Nb^{4+}$ ($g \approx 1.97$)[76].

It is noteworthy that in DRS spectra (see in the following, Section 3.6) the N,Nb-doped samples show systematically a larger absorption centered around 500 nm with respect to N-doped samples. Such a larger absorption might be related to an increased solubility of N in the host lattice as Nb incorporation increased[24]. Thus, although a larger amount of N-dopant is incorporated in the $TiO_2$ lattice in N,Nb-codoped samples, the occurrence of charge compensation between N and Nb results in a decrease of the N bulk paramagnetic species.

### 3.6 Visible absorption properties

Comparing the DRS results of single doped N- or Nb-containing materials with the N,Nb-codoped ones provides hints on the mutual role of the guest species in determining the photoabsorption properties of the nanopowders.

Doping with only Nb gives rise to a red shift of the absorption edge (Figure 10a), which results in a reduction of the observed band gap of about 0.2 eV (Table 1, 4$^{th}$ column). Literature studies reported similar red shift effects for Nb-doped $TiO_2$[38, 58], although in some cases a blue shift of the

absorption edge was also reported[23, 38]. Such a blue shift effect is generally attributed to the Burstein–Moss effect,[61] in which the conduction band filling by "extra" electrons due to Nb defects suppresses absorption at the band edge.

The situation is different in the case of N-doping. N-doped samples absorb in the visible region around 450-500 nm, but their absorption edge is comparable to that of undoped $TiO_2$ (Figure 10a). The visible light absorbance depends on the nominal nitrogen content of the material (Figure S13 SI), in agreement with previous reports[9-10, 15, 38].

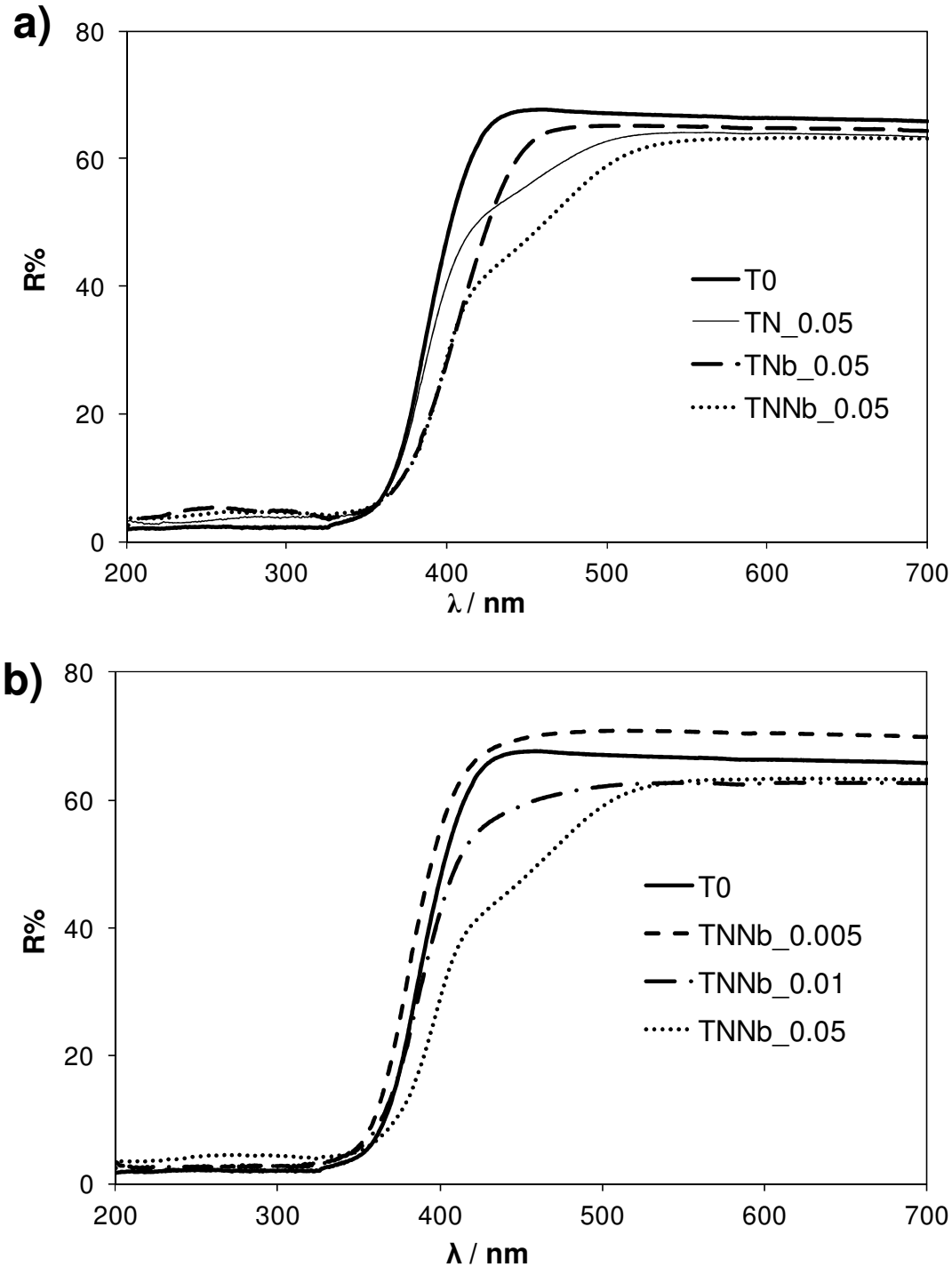


**Figure 10**. DRS spectra of a) undoped and 5% mono- and codoped samples; b) undoped and N,Nb-codoped $TiO_2$ samples at different dopant contents.

N,Nb-codoped materials show both an effect on the absorption edge (as Nb-doped samples) and a localized absorption in the visible region (as N-doped samples). Comparing TN_0.05, TNb_0.05 and TNNb_0.05 samples (Figure 10a), the latter presents both a red shift of the absorption edge and a "localized" absorption around 450 nm. The TNNb_0.05 sample shows indeed the lowest observed apparent band gap (2.93 eV vs. 3.09 eV for TN_0.05) (Table 2, 4$^{th}$ column). Interestingly, the visible absorption at 450 nm is significantly more intense in the codoped sample than in the case of the corresponding N-doped sample. Both effects (red shift and absorption at 450 nm) are appreciable in the case of the codoped powder with the intermediate dopant content (TNNb_0.01), while at low N,Nb-content (TNNb_0.005) a blue shift of the absorption edge is instead observed (Figure 10b).

While the occurrence of the visible absorption of N-doped samples can be traced back to the formation of shallow intra-gap states located above the valence band of $TiO_2$[9, 43, 69], the red shift detected in Nb-doped systems can be related, on the grounds of theoretical calculations, to the formation of donor levels located close to the conduction band (see Section 3.2 above). Lim *et al.*[38] reported similar results in the case of N,Nb-codoped samples. They attributed the increased absorption around 450 nm to a higher effective concentration of N in the $TiO_2$ lattice, in accordance with theoretical calculations reporting that codoping with transition metals (Nb, Ta) might facilitate the enhancement of the concentration of p-type dopants (N and C) in the host lattice[24]. Our optical analyses support this picture, but we go a step further by demonstrating that bulk electrons originating from Nb dopants can be localized onto N centers, making therefore available more charge density to be promoted into the CB upon visible-light photoexcitation.

## CONCLUSIONS

In this work, a thorough multi-disciplinary investigation has been carried out on N, Nb codoped multiphasic $TiO_2$-based nanostructured materials. The effects of both mono- and codoping

with N and Nb on the electronic, crystallographic and morphological properties of $TiO_2$ were studied through experimental (HR-XRPD, EXAFS, EDX, BET, SEM, EPR, DRS) and theoretical (plane-wave periodic DFT+U) methods. This joint experimental and theoretical approach has allowed us, on one hand, to probe the materials (micro)structure at both the local and the long-range scale. On the other hand, it has resulted in the development of a solid first-principle interpretative basis for the observed light-induced responses as a function of the doping strategy.

We found that N, Nb species give rise to a significant synergism determining both intensive and extensive properties of the nanopowders, while single N and Nb dopants are essentially ineffective at the very low (N, Nb / Ti $\leq$ 0.05) nominal loadings here employed. In particular, the contemporary presence of the two dopants implies a strong thermodynamic driving force toward the $TiO_2$-anatase phase, that results in the growth of smaller crystallites and particles with higher surface areas than in the undoped material.

Most important, EXAFS, HR-XRPD and DFT simulations provide compelling evidence that in N,Nb-codoped $TiO_2$ Nb enters the anatase lattice in substitutional position, confirming what in the literature is generally empirically attributed on the grounds of considerations of the similar ionic radii of the two ions. We also demonstrated that, at variance with interstitial Nb, substitutional Nb can transfer an electron to low-energy valence states of the N codopant near the valence band. This intrinsic charge compensation mechanism is substantiated by EPR measurements, that show a neat reduction of the signal due to paramagnetic bulk N species when Nb is also present in the lattice and the systematic disappearance of the E peak attributed to $Ti^{3+}$ species.

DRS measurements showed that N,Nb-codoped samples are subject to two distinct changes with respect to the undoped material, namely a slight shift of the band edge (either a blue or a red shift, depending on the dopant content) and an increased tendency to absorb visible photons in the region around 450-500 nm. We demonstrated that these two effects are individually due to Nb and N guests, respectively. When both the dopants are in the lattice, the absorbance around $\approx$ 450 nm is

significantly increased with respect to nitrogen-only containing nanopowders at comparable nominal N/Ti concentrations.

DFT calculations provide a solid interpretative basis to this synergistic behavior. Niobium and nitrogen create shallow mid-gap states near the conduction and valence bands, respectively, determining an overall (slight) reduction of the band gap. At the same time, substitutional Nb ions transfer charge density to guest N, dampening bulk paramagnetism and injecting electrons in states near the top of the valence band. These electrons can in turn contribute to the light absorption process, therefore enhancing the DRS response. The charge compensation mechanism can thus contribute to improve the photocatalytic activity of the $TiO_2$ under visible irradiation by both promoting the visible light absorption and reducing recombination processes.

The present work provides a comprehensive picture of how crystal structure, local coordination geometry, phase / defect composition and band structure are intertwined with each other in determining the structural properties and visible-light response of this class of important nanostructured materials.

**ACKNOWLEDGEMENTS**

Thanks are due to the European Synchrotron Radiation Facility (ESRF) for beamtime provision and to Dr. P. Abdala at SNBL for her experimental support. We acknowledge the CINECA and the Regione Lombardia award under the LISA initiative “MATGREEN”, for the availability of high performance computing resources and support. Partial funding by the Danish National Research Foundation (DNRF) through the Center for Materials Crystallography (CMC) has been also very much appreciated.

**Supporting Information Available:** Details of the X-ray powder diffraction experiments. EDX results. Full list of HR-XRPD results. BET adsorption isotherms of the mono-doped samples,

correlation between surface areas and crystallite size, and pore volume distributions of all samples. Refined unit cell parameters and Fermi Energies from PAW DFT simulations. DOS schemes for doping scenarios including oxygen vacancies. Full discussion on the EXAFS experiments. EPR results of N,Nb-codoped samples at different dopant contents. DRS spectra of single-doped samples. This material is available free of charge via the Internet at http://pubs.acs.org

## REFERENCES


1. Carp, O. Photoinduced Reactivity of Titanium Dioxide. *Prog. Solid State Chem.* **2004**, *32*, 33-177.

2. Chen, X.; Mao, S. S. Titanium Dioxide Nanomaterials: Synthesis, Properties, Modifications, and Applications. *Chem. Rev.* **2007**, *107*, 2891-2959.

3. Fujishima, A.; Zhang, X.; Tryk, D. Tio2 Photocatalysis and Related Surface Phenomena. *Surf. Sci. Rep.* **2008**, *63*, 515-582.

4. Meroni, D.; Ardizzone, S.; Cappelletti, G.; Ceotto, M.; Ratti, M.; Annunziata, R.; Benaglia, M.; Raimondi, L. Interplay between Chemistry and Texture in Hydrophobic Tio2hybrids. *J. Phys. Chem. C* **2011**, *115*, 18649-18658.

5. Spadavecchia, F.; Cappelletti, G.; Ardizzone, S.; Ceotto, M.; Azzola, M. S.; Lo Presti, L.; Cerrato, G.; Falciola, L. Role of Pr on the Semiconductor Properties of Nanotitania. An Experimental and First-Principles Investigation. *J. Phys. Chem. C* **2012**, *116*, 23083-23093.

6. Asahi, R. Visible-Light Photocatalysis in Nitrogen-Doped Titanium Oxides. *Science* **2001**, *293*, 269-271.

7. Zhang, J.; Wu, Y.; Xing, M.; Leghari, S. A. K.; Sajjad, S. Development of Modified N Doped Tio2 Photocatalyst with Metals, Nonmetals and Metal Oxides. *Ener. Environ. Sci.* **2010**, *3*, 715.

8. Lo Presti, L.; Ceotto, M.; Spadavecchia, F.; Cappelletti, G.; Meroni, D.; Acres, R. G.; Ardizzone, S. Role of the Nitrogen Source in Determining Structure and Morphology of N-Doped Nanocrystalline Tio2. *J. Phys. Chem. C* **2014**, *118*, 4797-4807.

9. Meroni, D.; Ardizzone, S.; Cappelletti, G.; Oliva, C.; Ceotto, M.; Poelman, D.; Poelman, H. Photocatalytic Removal of Ethanol and Acetaldehyde by N-Promoted Tio2 Films: The Role of the Different Nitrogen Sources. *Catal. Today* **2011**, *161*, 169-174.

10. Livraghi, S.; Paganini, M. C.; Giamello, E.; Selloni, A.; Di Valentin, C.; Pacchioni, G. Origin of Photoactivity of Nitrogen-Doped Titanium Dioxide under Visible Light. *J. Am. Chem. Soc.* **2006**, *128*, 15666-15671.

11. Spadavecchia, F.; Cappelletti, G.; Ardizzone, S.; Ceotto, M.; Falciola, L. Electronic Structure of Pure and N-Doped Tio2 Nanocrystals by Electrochemical Experiments and First Principles Calculations. *J. Phys. Chem. C* **2011**, *115*, 6381-6391.

12. Emeline, A. V.; Kuznetsov, V. N.; Rybchuk, V. K.; Serpone, N. Visible-Light-Active Titania Photocatalysts: The Case of N-Doped Tio2s—Properties and Some Fundamental Issues. *Int. J. Photoen.* **2008**, *2008*, 1-19.

13. Yates, H. M.; Nolan, M. G.; Sheel, D. W.; Pemble, M. E. The Role of Nitrogen Doping on the Development of Visible Light-Induced Photocatalytic Activity in Thin Tio2 Films Grown on Glass by Chemical Vapour Deposition. *J. Photochem. Photobiol., A* **2006**, *179*, 213-223.

14. Spadavecchia, F.; Cappelletti, G.; Ardizzone, S.; Bianchi, C. L.; Cappelli, S.; Oliva, C.; Scardi, P.; Leoni, M.; Fermo, P. Solar Photoactivity of Nano-N-Tio2 from Tertiary Amine: Role of Defects and Paramagnetic Species. *Appl. Catal., B* **2010**, *96*, 314-322.

15. Spadavecchia, F.; Ardizzone, S.; Cappelletti, G.; Oliva, C.; Cappelli, S. Time Effects on the Stability of the Induced Defects in Tio2 Nanoparticles Doped by Different Nitrogen Sources. *J. Nanopart. Res.* **2012**, *14*.

16. Taylor, S.; Mehta, M.; Samokhvalov, A. Production of Hydrogen by Glycerol Photoreforming Using Binary Nitrogen-Metal-Promoted N-M-Tio2photocatalysts. *ChemPhysChem* **2014**, *15*, 942-949.

17. Castro, A. L.; Nunes, M. R.; Carvalho, M. D.; Ferreira, L. P.; Jumas, J. C.; Costa, F. M.; Florêncio, M. H. Doped Titanium Dioxide Nanocrystalline Powders with High Photocatalytic Activity. *J. Solid State Chem.* **2009**, *182*, 1838-1845.

18. Cottineau, T.; Béalu, N.; Gross, P.-A.; Pronkin, S. N.; Keller, N.; Savinova, E. R.; Keller, V. One Step Synthesis of Niobium Doped Titania Nanotube Arrays to Form (N,Nb) Co-Doped Tio2 with High Visible Light Photoelectrochemical Activity. *J. Mater. Chem. A* **2013**, *1*, 2151.

19. Kudo, A.; Niishiro, R.; Iwase, A.; Kato, H. Effects of Doping of Metal Cations on Morphology, Activity, and Visible Light Response of Photocatalysts. *Chem. Phys.* **2007**, *339*, 104-110.

20. Furubayashi, Y.; Hitosugi, T.; Yamamoto, Y.; Inaba, K.; Kinoda, G.; Hirose, Y.; Shimada, T.; Hasegawa, T. A Transparent Metal: Nb-Doped Anatase Tio2. *Appl. Phys. Lett.* **2005**, *86*, 252101.

21. Hitosugi, T.; Yamada, N.; Nakao, S.; Hirose, Y.; Hasegawa, T. Properties of Tio2-Based Transparent Conducting Oxides. *Physica Status Solidi A* **2010**, *207*, 1529-1537.

22. Lü, X.; Mou, X.; Wu, J.; Zhang, D.; Zhang, L.; Huang, F.; Xu, F.; Huang, S. Improved-Performance Dye-Sensitized Solar Cells Using Nb-Doped Tio2electrodes: Efficient Electron Injection and Transfer. *Adv. Funct. Mater.* **2010**, *20*, 509-515.

23. Chandiran, A. K.; Sauvage, F. d. r.; Casas-Cabanas, M.; Comte, P.; Zakeeruddin, S. M.; Graetzel, M. Doping a Tio2 Photoanode with Nb5+ to Enhance Transparency and Charge Collection Efficiency in Dye-Sensitized Solar Cells. *J. Phys. Chem. C* **2010**, *114*, 15849-15856.

24. Ma, X.; Wu, Y.; Lu, Y.; Xu, J.; Wang, Y.; Zhu, Y. Effect of Compensated Codoping on the Photoelectrochemical Properties of Anatase Tio2photocatalyst. *J. Phys. Chem. C* **2011**, *115*, 16963-16969.

25. Zhao, Z.; Liu, Q. Designed Highly Effective Photocatalyst of Anatase Tio2 Codoped with Nitrogen and Vanadium under Visible-Light Irradiation Using First-Principles. *Catal. Lett.* **2008**, *124*, 111-117.

26. Gai, Y.; Li, J.; Li, S.-S.; Xia, J.-B.; Wei, S.-H. Design of Narrow-Gap Tio2: A Passivated Codoping Approach for Enhanced Photoelectrochemical Activity. *Phys. Rev. Lett.* **2009**, *102*, 036402.

27. Kuvarega, A. T.; Krause, R. W. M.; Mamba, B. B. Nitrogen/Palladium-Codoped Tio2 for Efficient Visible Light Photocatalytic Dye Degradation. *J. Phys. Chem. C* **2011**, *115*, 22110-22120.

28. Wang, X.; Tang, Y.; Leiw, M.-Y.; Lim, T.-T. Solvothermal Synthesis of Fe–C Codoped Tio2 Nanoparticles for Visible-Light Photocatalytic Removal of Emerging Organic Contaminants in Water. *Appl. Catal., A* **2011**, *409–410*, 257-266.

29. Thind, S. S.; Wu, G.; Chen, A. Synthesis of Mesoporous Nitrogen–Tungsten Co-Doped Tio2 Photocatalysts with High Visible Light Activity. *Appl. Catal., B* **2012**, *111–112*, 38-45.

30. Zhu, W.; Qiu, X.; Iancu, V.; Chen, X.-Q.; Pan, H.; Wang, W.; Dimitrijevic, N.; Rajh, T.; Meyer, H.; Paranthaman, M., et al. Band Gap Narrowing of Titanium Oxide Semiconductors by Noncompensated Anion-Cation Codoping for Enhanced Visible-Light Photoactivity. *Phys. Rev. Lett.* **2009**, *103*.

31. Wang, P.; Liu, Z.; Lin, F.; Zhou, G.; Wu, J.; Duan, W.; Gu, B.-L.; Zhang, S. B. Optimizing Photoelectrochemical Properties of Tio_{2} by Chemical Codoping. *Phys. Rev. B: Condens. Matter* **2010**, *82*.

32. Kurtoglu, M. E.; Longenbach, T.; Sohlberg, K.; Gogotsi, Y. Strong Coupling of Cr and N in Cr–N-Doped Tio2 and Its Effect on Photocatalytic Activity. *J. Phys. Chem. C* **2011**, *115*, 17392-17399.

33. Márquez, A. M.; Plata, J. J.; Ortega, Y.; Sanz, J. F.; Colón, G.; Kubacka, A.; Fernández-García, M. Making Photo-Selective Tio2 Materials by Cation–Anion Codoping: From Structure and Electronic Properties to Photoactivity. *J. Phys. Chem. C* **2012**, *116*, 18759-18767.

34. Gu, D.-E.; Yang, B.-C.; Hu, Y.-D. V and N Co-Doped Nanocrystal Anatase Tio2 Photocatalysts with Enhanced Photocatalytic Activity under Visible Light Irradiation. *Catal. Commun.* **2008**, *9*, 1472-1476.

35. Cong, Y.; Zhang, J.; Chen, F.; Anpo, M.; He, D. Preparation, Photocatalytic Activity, and Mechanism of Nano-Tio2 Co-Doped with Nitrogen and Iron (Iii). *J. Phys. Chem. C* **2007**, *111*, 10618-10623.

36. Breault, T. M.; Bartlett, B. M. Lowering the Band Gap of Anatase-Structured Tio2by Coalloying with Nb and N: Electronic Structure and Photocatalytic Degradation of Methylene Blue Dye. *J. Phys. Chem. C* **2012**, *116*, 5986-5994.

37. Breault, T. M.; Bartlett, B. M. Composition Dependence of Tio2:(Nb,N)-Xcompounds on the Rate of Photocatalytic Methylene Blue Dye Degradation. *J. Phys. Chem. C* **2013**, *117*, 8611-8618.

38. Lim, J.; Murugan, P.; Lakshminarasimhan, N.; Kim, J. Y.; Lee, J. S.; Lee, S.-H.; Choi, W. Synergic Photocatalytic Effects of Nitrogen and Niobium Co-Doping in Tio2 for the Redox Conversion of Aquatic Pollutants under Visible Light. *J. Catal.* **2014**, *310*, 91-99.

39. Toby, B. H. Expgui, a Graphical User Interface for Gsas. *J. Appl. Crystallogr.* **2001**, *34*, 210-213.

40. Larson, A. C.; Von Dreele, R. B. *General Structural Analysis System (Gsas)*; Los Alamos National Laboratory Report: LAUR, 2004.

41. Ravel, B.; Newville, M. Athena,Artemis,Hephaestus: Data Analysis for X-Ray Absorption Spectroscopy Usingifeffit. *J. Synchrotron Rad.* **2005**, *12*, 537-541.

42. Newville, M. Ifeffit : Interactive Xafs Analysis and Feff Fitting. *J. Synchrotron Rad.* **2001**, *8*, 322-324.

43. Ceotto, M.; Lo Presti, L.; Cappelletti, G.; Meroni, D.; Spadavecchia, F.; Zecca, R.; Leoni, M.; Scardi, P.; Bianchi, C. L.; Ardizzone, S. About the Nitrogen Location in Nanocrystalline N-Doped Tio2: Combined Dft and Exafs Approach. *J. Phys. Chem. C* **2012**, *116*, 1764-1771.

44. Kresse, G.; Hafner, J. Abinitio Molecular-Dynamics for Liquid-Metals. *Phys. Rev. B: Condens. Matter* **1993**, *47*, 558-561.

45. Kresse, G.; Furthmuller, J. Efficient Iterative Schemes for Ab Initio Total-Energy Calculations Using a Plane-Wave Basis Set. *Phys. Rev. B: Condens. Matter* **1996**, *54*, 11169-11186.

46. Blöchl, P. E. Projector Augmented-Wave Method. *Phys. Rev. B: Condens. Matter* **1994**, *50*, 17953-17979.

47. Kresse, G.; Joubert, D. From Ultrasoft Pseudopotentials to the Projector Augmented-Wave Method. *Phys. Rev. B: Condens. Matter* **1999**, *59*, 1758-1775.

48. Perdew, J. P.; Burke, K.; Ernzerhof, M. Generalized Gradient Approximation Made Simple. *Phys. Rev. Lett.* **1996**, *77*, 3865-3868.

49. Kresse, G.; Hafner, J. Ab Initio Molecular-Dynamics Simulation of the Liquid-Metal–Amorphous-Semiconductor Transition in Germanium. *Phys. Rev. B: Condens. Matter* **1994**, *49*, 14251-14269.

50. Perdew, J. P.; Wang, Y. Accurate and Simple Analytic Representation of the Electron-Gas Correlation-Energy. *Phys. Rev. B: Condens. Matter* **1992**, *45*, 13244-13249.

51. Teter, M. P.; Payne, M. C.; Allan, D. C. Solution of Schrödinger's Equation for Large Systems. *Phys. Rev. B: Condens. Matter* **1989**, *40*, 12255-12263.

52. Bylander, D. M.; Kleinman, L.; Lee, S. Self-Consistent Calculations of the Energy Bands and Bonding Properties of B12c3. *Phys. Rev. B: Condens. Matter* **1990**, *42*, 1394-1403.

53. Dudarev, S. L.; Botton, G. A.; Savrasov, S. Y.; Humphreys, C. J.; Sutton, A. P. Electron-Energy-Loss Spectra and the Structural Stability of Nickel Oxide: An Lsda+U Study. *Phys. Rev. B: Condens. Matter* **1998**, *57*, 1505-1509.

54. Mattioli, G.; Filippone, F.; Alippi, P.; Amore Bonapasta, A. Ab Initio Study of the Electronic States Induced by Oxygen Vacancies in Rutile and Anatase Tio2. *Phys. Rev. B: Condens. Matter* **2008**, *78*.

55. Morgan, B. J.; Watson, G. W. A Dft+U Description of Oxygen Vacancies at the Tio2 Rutile (110) Surface. *Surf. Sci.* **2007**, *601*, 5034-5041.

56. Cheng, H.; Selloni, A. Energetics and Diffusion of Intrinsic Surface and Subsurface Defects on Anatase Tio2(101). *J. Chem. Phys.* **2009**, *131*, 054703.

57. Stausholm-Møller, J.; Kristoffersen, H. H.; Hinnemann, B.; Madsen, G. K. H.; Hammer, B. r. Dft+U Study of Defects in Bulk Rutile Tio2. *J. Chem. Phys.* **2010**, *133*, 144708.

58. Biedrzycki, J.; Livraghi, S.; Giamello, E.; Agnoli, S.; Granozzi, G. Fluorine- and Niobium-Doped Tio2: Chemical and Spectroscopic Properties of Polycrystalline N-Type-Doped Anatase. *J. Phys. Chem. C* **2014**, *118*, 8462-8473.

59. Cheetham, A. K.; Rao, C. N. R. A Neutron Diffraction Study of Niobium Dioxide. *cta Crystallogr., Sect. B: Struct. Sci., Cryst. Eng. Mater.* **1976**, *32*, 1579-1580.

60. Furukawa, S.; Shishido, T.; Teramura, K.; Tanaka, T. Photocatalytic Oxidation of Alcohols over Tio2covered with Nb2o5. *ACS Catal.* **2012**, *2*, 175-179.

61. De Trizio, L.; Buonsanti, R.; Schimpf, A. M.; Llordes, A.; Gamelin, D. R.; Simonutti, R.; Milliron, D. J. Nb-Doped Colloidal Tio2 Nanocrystals with Tunable Infrared Absorption. *Chem. Mater.* **2013**, *25*, 3383-3390.

62. Mullin, J. W. *Crystallization*; Butterworth-Heinemann: Oxford (UK), 2001.

63. Anh Huy, H.; Aradi, B. l.; Frauenheim, T.; Deák, P. Comparison of Nb- and Ta-Doping of Anatase Tio2 for Transparent Conductor Applications. *J. Appl. Phys.* **2012**, *112*, 016103.

64. Di Valentin, C.; Pacchioni, G.; Selloni, A. Reduced and N-Type Doped Tio2: Nature of Ti3+ Species. *J. Phys. Chem. C* **2009**, *113*, 20543-20552.

65. Morgan, B. J.; Scanlon, D. O.; Watson, G. W. Small Polarons in Nb- and Ta-Doped Rutile and Anatase Tio2. *J. Mater. Chem.* **2009**, *19*, 5175.

66. Long, R.; English, N. J. Electronic Properties of Anatase-Tio2 Codoped by Cation-Pairs from Hybrid Density Functional Theory Calculations. *Chem. Phys. Lett.* **2011**, *513*, 218-223.

67. Morris, D.; Dou, Y.; Rebane, J.; Mitchell, C. E. J.; Egdell, R. G.; Law, D. S. L.; Vittadini, A.; Casarin, M. Photoemission and Stm Study of the Electronic Structure of Nb-Doped Tio2. *Phys. Rev. B: Condens. Matter* **2000**, *61*, 13445-13457.

68. Hitosugi, T.; Kamisaka, H.; Yamashita, K.; Nogawa, H.; Furubayashi, Y.; Nakao, S.; Yamada, N.; Chikamatsu, A.; Kumigashira, H.; Oshima, M., et al. Electronic Band Structure of Transparent Conductor: Nb-Doped Anatase Tio2. *Applied Physics Express* **2008**, *1*, 111203.

69. Di Valentin, C.; Finazzi, E.; Pacchioni, G.; Selloni, A.; Livraghi, S.; Paganini, M. C.; Giamello, E. N-Doped Tio2: Theory and Experiment. *Chem. Phys.* **2007**, *339*, 44-56.

70. Howard, C. J.; Sabine, T. M.; Dickson, F. Structural and Thermal Parameters for Rutile and Anatase. *cta Crystallogr., Sect. B: Struct. Sci., Cryst. Eng. Mater.* **1991**, *47*, 462-468.

71. Shannon, R. Revised Effective Ionic Radii and Systematic Studies of Interatomic Distances in Halides and Chalcogenides. *Acta Crystallogr., Sect. A: Found. Adv.* **1976**, *32*, 751-767.

72. Bouchet, R.; Weibel, A.; Knauth, P.; Mountjoy, G.; Chadwick, A. V. Exafs Study of Dopant Segregation (Zn, Nb) in Nanocrystalline Anatase (Tio2). *Chem. Mater.* **2003**, *15*, 4996-5002.

73. Nowotny, M. K.; Sheppard, L. R.; Bak, T.; Nowotny, J. Defect Chemistry of Titanium Dioxide. Application of Defect Engineering in Processing of Tio2-Based Photocatalysts†. *J. Phys. Chem. C* **2008**, *112*, 5275-5300.

74. Howe, R. F.; Gratzel, M. Epr Observation of Trapped Electrons in Colloidal Titanium Dioxide. *J. Phys. Chem.* **1985**, *89*, 4495-4499.

75. Livraghi, S.; Chiesa, M.; Paganini, M. C.; Giamello, E. On the Nature of Reduced States in Titanium Dioxide as Monitored by Electron Paramagnetic Resonance. I: The Anatase Case. *J. Phys. Chem. C* **2011**, *115*, 25413-25421.

76. Kiwi, J.; Suss, J. T.; Szapiro, S. Epr Spectra of Niobium-Doped Tio2 and Imiplications for Water Photocleavage Processes. *Chem. Phys. Lett.* **1984**, *106*, 135-138.

**Table of contents**